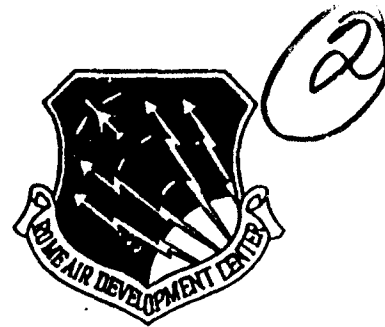


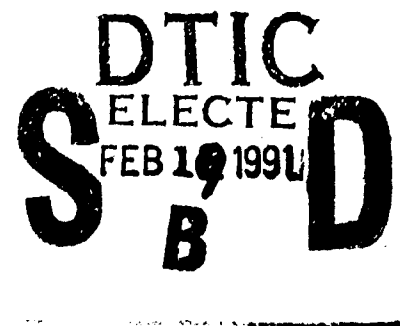
RADC-TR-90-301
Interim Technical Report
November 1990



NON-SPECULAR SCATTERING FROM ROUGHENED ALUMINUM SURFACES

University of Lowell

G. Phillips, Z. Fried, J. Waldman



APPROVED FOR PUBLIC RELEASE; DISTRIBUTION UNLIMITED.

91 2 13 109

Rome Air Development Center
Air Force Systems Command
Griffiss Air Force Base, NY 13441-5700

AD-A231 824

This report has been reviewed by the RADC Public Affairs Division (PA) and is releasable to the National Technical Information Service (NTIS). At NTIS it will be releasable to the general public, including foreign nations.

RADC-TR-90-301 has been reviewed and is approved for publication.

APPROVED:



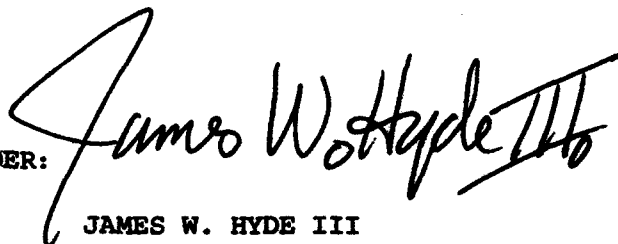
K. V. N. RAO
Project Engineer

APPROVED:



JOHN K. SCHINDLER
Director of Electromagnetics

FOR THE COMMANDER:



JAMES W. HYDE III
Directorate of Plans & Programs

If your address has changed or if you wish to be removed from the RADC mailing list, or if the addressee is no longer employed by your organization, please notify RADC (EEC) Hanscom AFB MA 01731-5000. This will assist us in maintaining a current mailing list.

Do not return copies of this report unless contractual obligations or notices on a specific document require that it be returned.

REPORT DOCUMENTATION PAGE

Form Approved
OMB No. 0704-0188

Public reporting burden for this collection of information is estimated to average 1 hour per response, including the time for reviewing instructions, searching existing data sources, gathering and maintaining the data needed, and completing and reviewing the collection of information. Send comments regarding this burden estimate or any other aspect of this collection of information, including suggestions for reducing this burden, to Washington Headquarters Services, Directorate for Information Operations and Reports, 1215 Jefferson Davis Highway, Suite 1204, Arlington, VA 22202-4302, and to the Office of Management and Budget, Paperwork Reduction Project (0704-0188), Washington, DC 20503.

| | | | | | |
|--|---|--|-----------------------------------|--|--|
| 1. AGENCY USE ONLY (Leave Blank) | | 2. REPORT DATE November 1990 | | 3. REPORT TYPE AND DATES COVERED Interim Dec 88 to Dec 90 | |
| 4. TITLE AND SUBTITLE NON-SPECULAR SCATTERING FROM ROUGHENED ALUMINUM SURFACES | | | | 5. FUNDING NUMBERS C - F19628-88-D-0020 PE - 61102F PR - 2305 TA - J4 WU - 38 | |
| 6. AUTHOR(S) G. Phillips, Z. Fried, J. Waldman | | | | | |
| 7. PERFORMING ORGANIZATION NAME(S) AND ADDRESS(ES) University of Lowell Research Foundation 650 Aiken St Lowell MA 01854 | | | | 8. PERFORMING ORGANIZATION REPORT NUMBER | |
| 9. SPONSORING/MONITORING AGENCY NAME(S) AND ADDRESS(ES) Rome Air Development Center (EEC) Hanscom AFB MA 01731-5000 | | | | 10. SPONSORING/MONITORING AGENCY REPORT NUMBER RADC-TR-90-301 | |
| 11. SUPPLEMENTARY NOTES RADC Project Engineer: K.V.N. Rao/EEC/(617)478-3106 | | | | | |
| 12a. DISTRIBUTION/AVAILABILITY STATEMENT Approved for public release; distribution unlimited | | | | 12b. DISTRIBUTION CODE | |
| 13. ABSTRACT (Maximum 200 words) Scattering of CO ₂ laser radiation off roughened aluminum surfaces was measured and compared to the predictions of Papa, Lennon and Taylor. The incident radiation was linearly polarized perpendicular to the incident plane, and the scattering was analyzed along two directions, parallel and perpendicular to the scattering plane. The experimental setup is described in detail and data are presented for several depression and aspect angles. | | | | | |
| 14. SUBJECT TERMS Rough Surfaces, Polarization Nulls, Electromagnetic Scattering, Depolarization, Rough Surface Scattering, Bistatic Polarization Nulls | | | | 15. NUMBER OF PAGES 36 | |
| | | | | 16. PRICE CODE | |
| 17. SECURITY CLASSIFICATION OF REPORT UNCLASSIFIED | 18. SECURITY CLASSIFICATION OF THIS PAGE UNCLASSIFIED | 19. SECURITY CLASSIFICATION OF ABSTRACT UNCLASSIFIED | 20. LIMITATION OF ABSTRACT SAR | | |

Abstract

Non specular scattering of CO₂ laser radiation off roughened aluminum surfaces was measured and compared to the predictions of Papa, Lennon, and Taylor. The incident radiation was linearly polarized perpendicular to the incident plane, and the scattering was analyzed along two directions, parallel and perpendicular to the scattering plane. The experimental setup is described in detail and data are presented for several depression and aspect angles.

Introduction

Scattering of electromagnetic radiation by rough surfaces has been the subject of great interest for several decades¹. Interest in this derives from a need to study terrain characteristics of inaccessible sites and to detect and characterize small deviations from optically smooth surfaces. In either case, the goals are to relate electromagnetic scattering data to the properties of the scattering surface. In principle, knowledge of the exact shape of the scattering surface and the total electric field at the surface allows one to compute the electric field at the point of observation. The exact solution is given by (1) where k is the magnitude of the wave vector of the incident radiation and R is the distance between some point on the illuminated surface and the observation point²:

$$E_2(P) = \frac{1}{4\pi} \int_s (E \frac{\partial \psi}{\partial n} - \psi \frac{\partial E}{\partial n}) dS \quad (1)$$

where

$$\psi = \frac{e^{ik \cdot R}}{|R|} \quad (2)$$

A cursory look at equation (1) immediately confronts one with the two fundamental obstacles to finding $E_2(P)$. One problem is that the exact shape of the surface is unknown. Secondly, given the detailed geometry of the surface, there still remains the problem of knowing the value of the total E on the surface, as given by (3).

$$E = E_i + E_s \quad (3)$$



Availability Codes

Avail and/or

Dist Special

A-1

E_i and E_s represent the incident and scattered electric fields on the surface, respectively. To obtain the value of E , one must solve the boundary conditions for both E and H at the surface. Unfortunately, closed form solutions for the latter problem exist only for plane surfaces. In the high frequency or geometrical optics (GO) limit, the ratio of scattered to incident electric field is the same as the corresponding quantities obtained from the Fresnel coefficients. Consequently, in the GO limit, this part of the problem is eliminated. The need to characterize the surface, however, remains. An exact mapping of the surface is an insurmountable task and may not be necessary. It is usually assumed that different microscopic surface shapes will yield similar scattering patterns, when illuminated over a sufficiently large area of the rough surface. The statistical characterization of rough surfaces is motivated by the need to obtain closed form expressions for $E_2(P)$ without detailed knowledge of the surface shape. A model in which one assumes the random distribution of hemispherical bosses³ and the tangent plane model (TP) are currently in use⁴. The TP approximation is the most straightforward approach. In the GO limit, all shapes can be handled by the TP approximation in which only the average surface slopes are of interest. To obtain a statistical representation of the surface, it is important that the illuminated area provides an adequate representation of the surface characteristics. Papa, Lennon, and Taylor⁵ have shown that for uncorrelated heights and slope distributions, in a Gaussian surface, the physical optics approach yields identical results to those obtained in the GO limit, provided that the correlation length T is much larger than the wavelength and the average slopes are significantly less than one. Another important observation of Papa, Lennon, and Taylor is that in the TP regime, the polarization of the scattered wave is independent of the detailed statistical properties of the surface. The primary objective of this work is to verify the predicted polarization behavior.

Previous measurements of rough surface scattering⁶ were performed in the monostatic configuration or under conditions where the scattered radiation was in the plane of incidence. Such an arrangement precludes the experimental study of some interesting features of polarization dependence. These manifest themselves only in configurations where the scattering plane is different from the incident plane. The apparatus utilized in this study, however, allows the measurement of scattered radiation in both the polar and azimuthal directions.

Data was collected under the following conditions. Laser radiation ($\lambda = 10.6\mu$) was incident on roughened aluminum surfaces at several depression and aspect angles and the co-pol and cross-pol scattering cross sections compared with the theoretical predictions of Papa, Lennon, and Taylor⁵. In their article, Papa, et.al.⁵, using a form of the scattering cross section given by Barrick⁴ (equation 4), describe the rather complicated angular dependences of σ_o as a function of polarization, surface roughness, and dielectric constant. Furthermore, their analysis shows that for a given incident signal polarization, there exists nulls in the co-pol and cross-pol scattering cross sections for various angles. The data set presented later in this report is shown to verify these predictions, at least for a subset of scattering angles. The scattering cross section is given by^{4,5}:

$$\sigma_o = |\beta_{pq}|^2 JS \quad (4)$$

As described by Barrick⁴, a specular point in the surface reflects like a tilted plane tangent to the surface at that point. The β_{pq} in equation (4) are given below in terms of the Fresnel coefficients for s and p waves and spherical scattering coordinates (see figure 1).

$$\beta_{VV} = \frac{a_2 a_3 R_{\parallel}(i) + \sin(\theta_i) \sin(\theta_s) \sin^2(\phi_s) R_{\perp}}{a_1 a_4} \quad (5)$$

$$\beta_{HV} = \frac{\sin \phi_s [-\sin \theta_i a_3 R_{\parallel}(i) + \sin \theta_s a_2 R_{\perp}(i)]}{a_1 a_4} \quad (6)$$

$$\beta_{VH} = \frac{\sin \phi_s [\sin \theta_s a_2 R_{\parallel}(i) + \sin \theta_i a_3 R_{\perp}(i)]}{a_1 a_4} \quad (7)$$

$$\beta_{HH} = \frac{-\sin \theta_i \sin \theta_s \sin^2 \phi_s R_{\parallel}(i) - a_2 a_3 R_{\perp}(i)}{a_1 a_4} \quad (8)$$

with

$$a_1 = 1 + \sin \theta_i \sin \theta_s \cos \phi_s - \cos \theta_i \cos \theta_s \quad (9)$$

$$a_2 = \cos \theta_i \sin \theta_s + \sin \theta_i \cos \theta_s \cos \phi_s \quad (10)$$

$$a_3 = \sin \theta_i \cos \theta_s + \cos \theta_i \sin \theta_s \cos \phi_s \quad (11)$$

$$a_4 = \cos \theta_i + \cos \theta_s \quad (12)$$

The angle (i) is the angle between the global surface normal and the local normal of the facet. It is defined below in terms of the scattering angles of figure 1.

$$\cos i = \frac{1}{\sqrt{2}}[1 - \sin \theta_i \sin \theta_s \cos \phi_s + \cos \theta_i \cos \theta_s] \quad (13)$$

In equation (4), the J term is proportional to the average number of facets having slopes which scatter into the observation direction. The shadowing function S gives the fraction of the total number of specular points not shadowed⁷. In the analysis of Papa, Lennon, and Taylor, it is pointed out that neither the shadowing function nor the slope statistical J term has an influence on the position of nulls in the scattering cross section. Thus, the predicted angular position of nulls in σ_0 as given by these authors is based solely on the behavior of $|\beta_{pq}|^2$ in equation (4). The data set presented in this report is given in two formats. One format is a plot of the ratio of co-pol and cross-pol data, $\left| \frac{\beta_{HH}}{\beta_{HV}} \right|^2$, and therefore is independent of the JS factors in equation (4). The other data set is a plot of the absolute normalized cross section $|\beta_{HH}|^2$ and includes the effect of JS in the scattering cross section.

Unlike smooth surfaces, roughened surfaces scatter in all directions. This requires the detector to be moveable over a hemisphere. Practical considerations, especially for a liquid nitrogen cooled IR (infrared) detector, limit the detector's motion to the horizontal plane in the laboratory. To insure accessibility of arbitrary scattering angles, the polar angle θ_s and particularly ϕ_s , the azimuthal angle, require that the target surface be free to rotate around two perpendicular axes. The correspondence between laboratory angles in which the mean surface normal changes direction, and the conventionally defined field angles is presented in section II. In section III the measurement apparatus and techniques used for data collection is described. In section IV we present data graphically and compare it to the theoretical model. A summary and conclusion is presented in section V.

II. Transformation of Coordinates between Lab and Field Frame

In the field frame, the target surface orientation is fixed and the transmit and receive directions (vectors) can vary independently over a hemisphere (see Figure 1). In this frame, we designate the following angles θ_i , θ_s , and ϕ_s . θ_i stands for the incident angle, the angle between the incident propagation direction and target normal.

$$\mathbf{r}_i \cdot \mathbf{n} = -\cos(\theta_i) \quad (14)$$

\mathbf{r}_i is a unit vector along the direction of propagation, and \mathbf{n} is a unit vector along the surface normal. Similarly,

$$\mathbf{r}_s \cdot \mathbf{n} = \cos(\theta_s) \quad (15)$$

where \mathbf{r}_s is a unit vector along the detector direction and

$$\frac{[\mathbf{r}_i - \mathbf{n}(\mathbf{r}_i \cdot \mathbf{n})]}{\sin(\theta_i)} \cdot \frac{[\mathbf{r}_s - \mathbf{n}(\mathbf{r}_s \cdot \mathbf{n})]}{\sin(\theta_s)} = \cos(\phi_s) \quad (16)$$

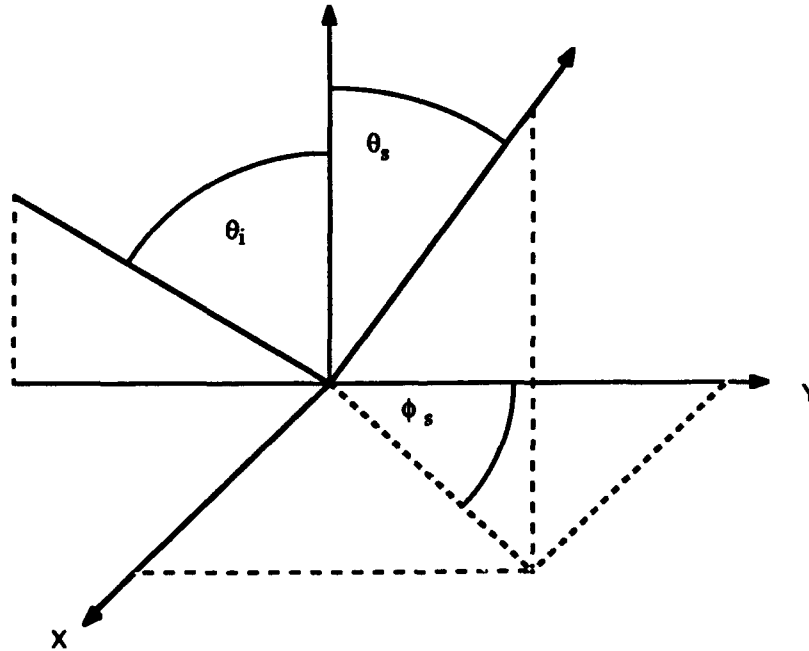


Figure 1. Definition of field angles

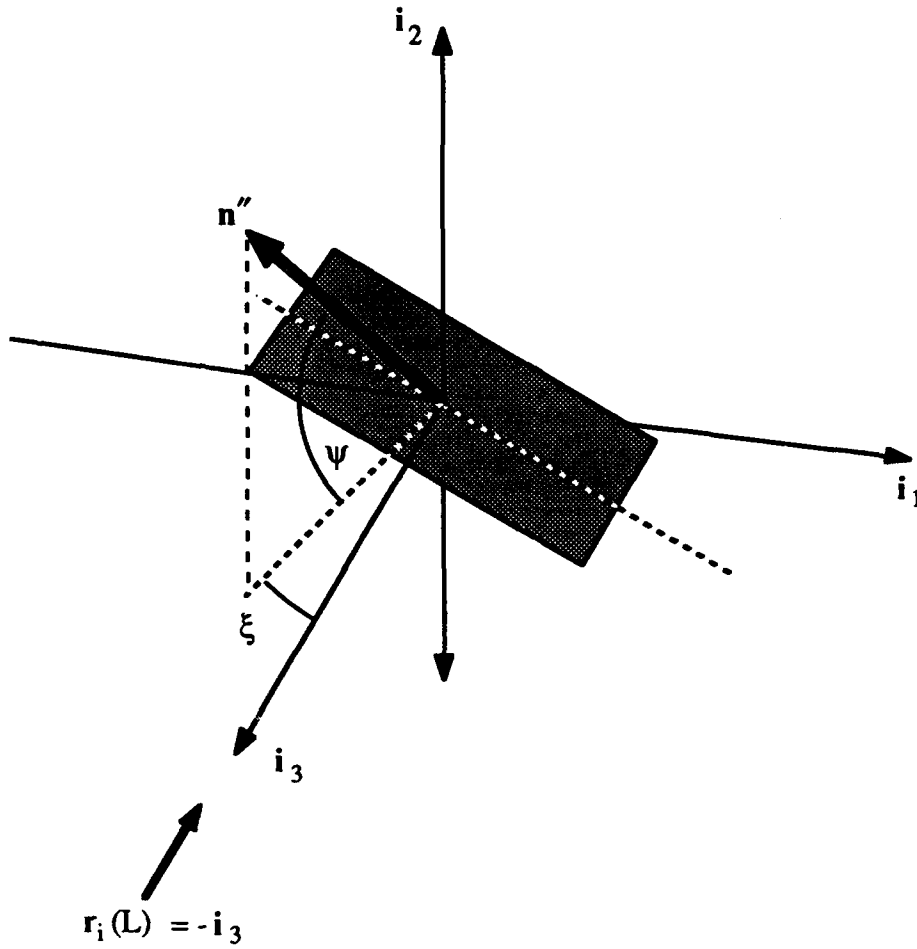


Figure 2. Definition of laboratory angles for $\xi \neq 0$ and $\psi \neq 0$

In the laboratory frame (Figure 2), the propagation direction is fixed, which is taken along the negative z-axis. Thus,

$$\mathbf{r}_i(L) = -\mathbf{i}_3 \quad (17)$$

where L designates the laboratory frame and \mathbf{i}_3 is a unit vector along the z-axis (Figure 2). The detector arm is in the x-z plane and can be rotated through 270° (Figure 3).

Hence

$$\mathbf{r}_D(L) = \cos(\eta) \mathbf{i}_1 + \sin(\eta) \mathbf{i}_3 \quad (18)$$

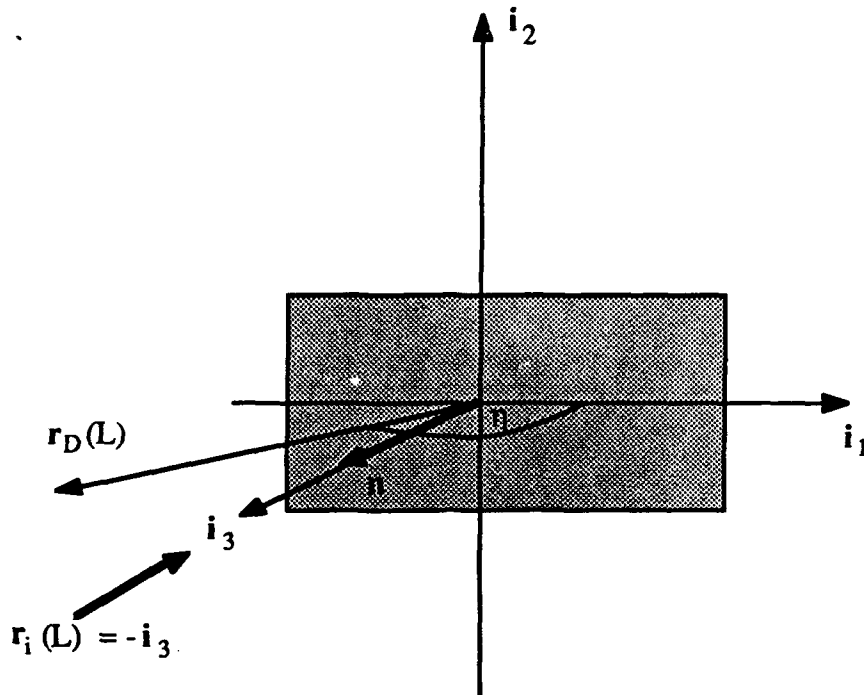


Figure 3. Laboratory system for $\psi = 0$ and $\xi = 0$ showing the detector position $r_D(L)$

The target surface normal can be rotated around two perpendicular axes. One rotation is around the y-axis (Figure 4), the axis perpendicular to the x-z plane containing the transmitter and receiver. The angle describing this rotation is designated by ξ . The range of ξ is from 0° to 90° . The detector arm requires a 180° range for any fixed ξ . Hence, the full range of the detector arm has to be 270° .

A second rotation can be performed around the line which is the intersection of the target plane and the x-z plane (Figure 2).

The first rotation fixes ξ and the second rotation fixes ψ . When the target surface is rotated through ξ and ψ in succession, the normal to the target surface, expressed in the unit vectors of the laboratory coordinate system is:

$$\mathbf{n}'' = -\mathbf{i}_1 \sin(\xi) \cos(\psi) + \mathbf{i}_2 \sin(\psi) + \mathbf{i}_3 \cos(\xi) \cos(\psi) \quad (19)$$

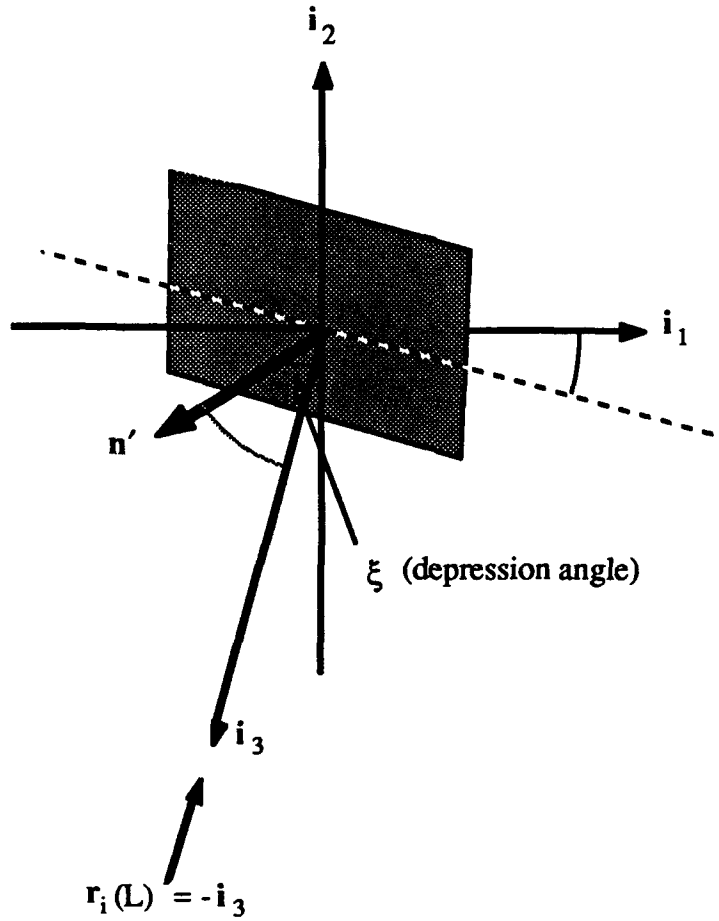


Figure 4. Laboratory system for $\xi \neq 0$ and $\psi = 0$

We note that the scalar products (14)-(16) defining the various field angles retain the same form when \mathbf{n}'' is substituted for \mathbf{n} . The following expressions relate laboratory angles (ξ, ψ, η) to field angles ($\theta_i, \theta_s, \phi_s$)

$$\cos(\theta_i) = -\mathbf{r}_i \cdot \mathbf{n}'' = \cos(\xi) \cos(\psi) \quad (20)$$

$$\cos(\theta_s) = \mathbf{r}_D \cdot \mathbf{n}'' = \sin(\eta - \xi) \cos(\psi) \quad (21)$$

and

$$\cos(\phi_s) = \frac{\mathbf{r}_i \cdot \mathbf{r}_D - (\mathbf{r}_i \cdot \mathbf{n}'')(\mathbf{r}_D \cdot \mathbf{n}'')}{\sqrt{1 - (\mathbf{r}_i \cdot \mathbf{n}'')^2} \sqrt{1 - (\mathbf{r}_D \cdot \mathbf{n}'')^2}} \quad (22)$$

Substituting equations (17), (18), (20) and (21) into Eqn. (22) yields:

$$\cos(\phi_s) = \frac{-\sin(\eta) + \cos^2(\psi) \sin(\xi - \eta) \cos(\xi)}{\sqrt{1 - \cos^2(\xi)} \cos^2(\psi) \sqrt{1 - \cos^2(\psi) \sin^2(\xi - \eta)}} \quad (23)$$

We proceed to show that for a fixed θ_i and θ_s both larger than 0° (0° is a point of degeneracy) $\cos(\phi_s)$ can assume all values between -1 and +1. denoting $\cos(\theta_i) = x$ and $\cos(\theta_s) = y$, Eqn. (23) can be written as:

$$\cos(\phi_s) = \frac{-\sin(\eta) + yx}{\sqrt{1 - x^2} \sqrt{1 - y^2}} \quad (24)$$

For a fixed ψ and ξ , η is not an independent variable. We therefore express $\sin(\eta)$ in terms of ξ , ψ .

$$\sin(\eta) = \sin(\eta - \xi + \xi) = \sin(\eta - \xi) \cos(\xi) + \cos(\eta - \xi) \sin(\xi) \quad (25)$$

or

$$\sin(\eta) = \frac{xy \pm \sqrt{[\cos^2(\psi) - y^2][\cos^2(\psi) - x^2]}}{\cos^2(\psi)} \quad (26)$$

The - sign in front of the square root has to be inserted when $(\eta - \xi) > 90^\circ$. Combining (23)-(26) one writes:

$$\cos(\phi_s) = \frac{-xy \tan^2 \psi \pm \sqrt{1 - \frac{y^2}{\cos^2 \psi}} \sqrt{1 - \frac{x^2}{\cos^2 \psi}}}{\sqrt{1 - y^2} \sqrt{1 - x^2}} \quad (27)$$

We first show that $\cos(\phi_s)$ can assume the extreme values of ± 1 . This can be seen by setting $\psi = 0$. The + sign in front of the square root yields +1, and the - sign yields -1. It is useful to rewrite the expression (14) as two equations each valid in a given range of $\cos(\phi_s)$. Assuming that $y > x$:

$$\text{Cos}(\phi_s) = \frac{-xy \tan^2 \psi + \sqrt{1 - \frac{y^2}{\text{Cos}^2 \psi}} \sqrt{1 - \frac{x^2}{\text{Cos}^2 \psi}}}{\sqrt{1 - y^2} \sqrt{1 - x^2}} \quad (28)$$

Eqn. (28) is valid for :

$$-\frac{x}{y} \sqrt{\frac{1 - y^2}{1 - x^2}} \leq \text{Cos}(\phi_s) \leq 1$$

and

$$\text{Cos}(\phi_s) = \frac{-xy \tan^2 \psi - \sqrt{1 - \frac{y^2}{\text{Cos}^2 \psi}} \sqrt{1 - \frac{x^2}{\text{Cos}^2 \psi}}}{\sqrt{1 - y^2} \sqrt{1 - x^2}} \quad (29)$$

Eqn. (29) is valid for :

$$-1 \leq \text{Cos}(\phi_s) \leq -\frac{x}{y} \sqrt{\frac{1 - y^2}{1 - x^2}}$$

For $x > y$, $-\frac{x}{y} \sqrt{\frac{1 - y^2}{1 - x^2}}$ must be replaced with $-\frac{y}{x} \sqrt{\frac{1 - x^2}{1 - y^2}}$. Since both functions are continuous functions of ψ , for $0 \leq \psi \leq \text{Cos}^{-1}(y)$, $\text{Cos}(\phi_s)$ assumes all values in between.

The algorithm for determining ξ , η , ψ for a given θ_i , θ_s , ϕ_s is as follows:

Compute $\text{Cos}(\phi_s)$ and select the larger of $\text{Cos}(\theta_s)$ or $\text{Cos}(\theta_i)$ thereby setting the appropriate range for equations (28) and (29). The value of $\text{Cos}(\phi_s)$ determines whether Eqn. (28) or (29) is to be used. Having selected the correct equation, one solves for $\text{Cos}(\psi)$ and determines ψ . Given $\text{Cos}(\psi)$, one then can determine $\text{Cos}(\xi)$ or ξ . η remains to be determined and is obtained from: $y = \text{Cos}(\theta_s) = \text{Sin}(\eta - \xi) \text{Cos}(\psi)$.

Since $\text{Sin}(\eta - \xi)$ is symmetric around 90° , a unique determination of η depends on whether Eqn. (28) or (29) was used. For Eqn. (28), $\eta - \xi \geq 90^\circ$ and for Eqn. (29) $\eta - \xi \leq 90^\circ$.

To complete this section, we write down the direction of linear polarization that corresponds to an H transmit state. It is given by:

$$\mathbf{r}_i \times \mathbf{n}'' = -i_1 \sin(\psi) + i_2 \sin(\xi) \cos(\psi) \quad (30)$$

An H receive state is given by:

$$\mathbf{r}_D \times \mathbf{n}'' = -[i_1 \sin(\eta) \cos(\xi) + i_2 \cos(\eta - \xi)] \cos(\psi) + i_3 \cos(\eta) \sin(\psi) \quad (31)$$

The V receive state is obtained from:

$$\mathbf{r}_D \times (\mathbf{r}_D \times \mathbf{n}'') = \mathbf{r}_D (\mathbf{r}_D \cdot \mathbf{n}'') - \mathbf{n}'' \quad (32)$$

or

$$\begin{aligned} \mathbf{r}_D \times (\mathbf{r}_D \times \mathbf{n}'') = & i_1 [\cos(\eta) \sin(\eta - \xi) + \sin(\xi)] \cos(\psi) \\ & + i_2 [\sin(\eta) \sin(\eta - \xi) \cos(\psi) - \sin(\psi)] - i_3 \cos(\xi) \cos(\psi) \end{aligned} \quad (33)$$

III. Laboratory Setup and Measuring Techniques

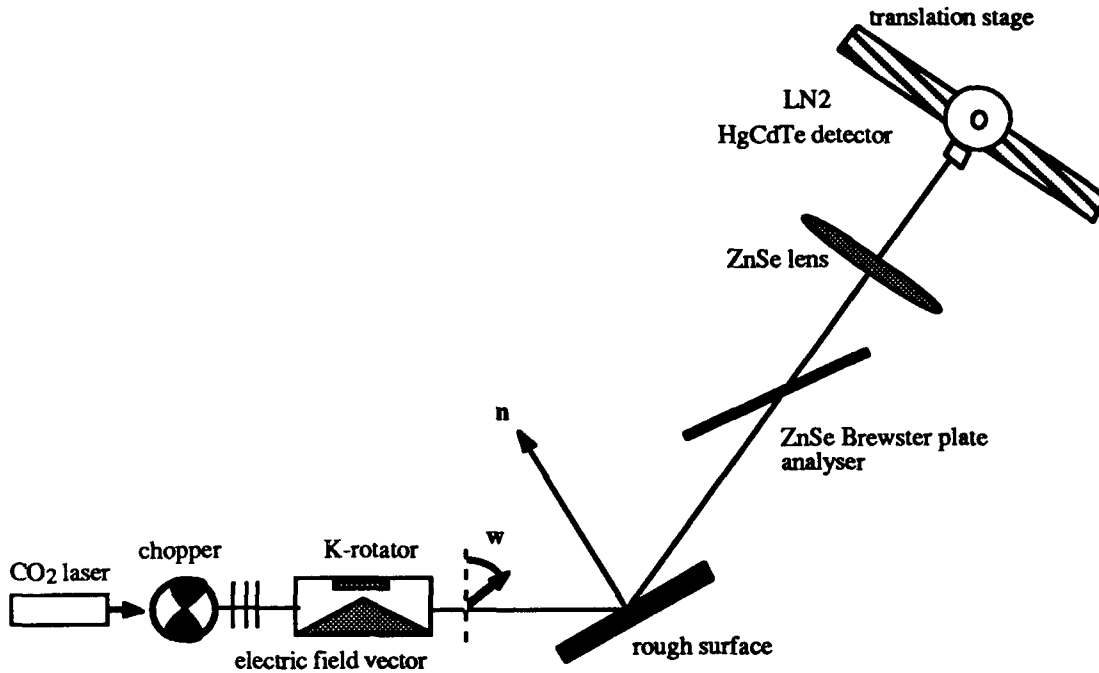


Figure 5.

The source of radiation is a CO₂ laser providing 10 watts of linearly polarized radiation tunable in a narrow band from 9.2 to 10.8 microns. The ability to rotate the polarization to any desired incident state is provided by a K-rotator. The rough surface is allowed to rotate through two degrees of freedom which, in conjunction with the position of the detector, simulates the environment of a bistatic radar in the field (the relationship between field and lab coordinates is provided in section II.). At the receive end, discrimination between polarization states is accomplished by rotating a Brewster plate analyzer. The radiation is collected by a two inch diameter ZnSe lens with a focal length of 20 inches. A liquid nitrogen cooled HgCdTe detector (detectivity = 10^{10} cm Hz^{1/2}/watt), mounted on a translation stage in the focal plane of the lens, scans the resultant intensity pattern. Scanning over a finite angular spread is necessitated by the scintillation pattern that results from the narrowband laser radiation scattering from the rough surface. The detector output is fed into a lock-in amplifier and the time averaged signal displayed on a strip chart recorder.

The results of these measurements are given later in the data section of this report. The data sets were collected by the following method. The incident and scattered angles (ξ_i and η) of the

roughened aluminum substrates are fixed at some value between 10° and 60° and are chosen to be equal. The angle ψ is then varied over a range such that the scattering cross section passes through a null as determined from the transformed scattering equation, $\sigma_o = |\beta_{pq}|^2 J^5$. The calculation of the position of the scattering null in terms of both field and lab coordinates, as well as the polarization rotation angles required is accomplished by computer. Table 1 displays the scanning parameters calculated for a bistatic measurement in terms of both the lab based angles, and the field coordinates. In the following sections the angles ξ and ψ are referred to as the (laboratory) depression and aspect angles, respectively.

For the parameter set given in Table 1, the depression angle ξ is fixed at 60° . As the aspect angle ψ is varied from 31° to 51° , a null in the calculated scattering cross section, σ , occurs at 41° . For every orientation of the surface in aspect and depression, an angle w is calculated which is the angle the polarization vector makes with the vertical to insure an H incident state. At the receive end of the system, to discriminate between HH and HV, the polarizer analyzer is set at angles corresponding to polarization states H and V, respectively. The measurements of HH and HV are ratioed and plotted along with the model prediction.

Table 1. Depression $\xi_i = \xi_s = 60^\circ$

| ψ | θ_i | θ_s | ϕ_s | $(\sigma_{hh}/\sigma_{hv})_{calc}$ |
|--------|------------|------------|----------|------------------------------------|
| 28 | 63.8 | 63.8 | 30.3 | 0.066 |
| 29 | 64.1 | 64.1 | 31.3 | 0.057 |
| 30 | 64.3 | 64.3 | 32.2 | 0.049 |
| 31 | 64.6 | 64.6 | 33.1 | 0.042 |
| 32 | 64.9 | 64.9 | 34.0 | 0.035 |
| 33 | 65.2 | 65.2 | 34.9 | 0.028 |
| 34 | 65.5 | 65.5 | 35.8 | 0.022 |
| 35 | 65.8 | 65.8 | 36.6 | 0.016 |
| 36 | 66.1 | 66.1 | 37.5 | 0.012 |
| 37 | 66.5 | 66.5 | 38.3 | 0.007 |
| 38 | 66.8 | 66.8 | 39.1 | 0.004 |
| 39 | 67.1 | 67.1 | 39.9 | 0.002 |
| 40 | 67.5 | 67.5 | 40.7 | 0.000 |
| 41 | 67.8 | 67.8 | 41.5 | 0.000 |
| 42 | 68.2 | 68.2 | 42.2 | 0.001 |
| 43 | 68.6 | 68.6 | 43.0 | 0.003 |
| 44 | 68.9 | 68.9 | 43.7 | 0.006 |
| 45 | 69.3 | 69.3 | 44.4 | 0.010 |
| 46 | 69.7 | 69.7 | 45.1 | 0.016 |
| 47 | 70.1 | 70.1 | 45.8 | 0.024 |
| 48 | 70.5 | 70.5 | 46.4 | 0.033 |
| 49 | 70.9 | 70.9 | 47.1 | 0.044 |
| 50 | 71.3 | 71.3 | 47.7 | 0.058 |
| 51 | 71.7 | 71.7 | 48.3 | 0.073 |
| 52 | 72.1 | 72.1 | 48.9 | 0.091 |
| 53 | 72.5 | 72.5 | 49.5 | 0.112 |
| 54 | 72.9 | 72.9 | 50.1 | 0.136 |
| 55 | 73.3 | 73.3 | 50.6 | 0.162 |
| 56 | 73.8 | 73.8 | 51.2 | 0.193 |
| 57 | 74.2 | 74.2 | 51.7 | 0.227 |
| 58 | 74.6 | 74.6 | 52.2 | 0.266 |
| 59 | 75.1 | 75.1 | 52.7 | 0.310 |
| 60 | 75.5 | 75.5 | 53.1 | 0.360 |

A sand blaster was used to roughen aluminum surfaces. The abrasive material used in preparing the surfaces was small glass beads ranging in diameter from 40 to 600 microns. The results of profilometer tracings indicate that the heavier abrasive materials produce facets that range

in depth from 5 to 30 microns. Average depths of 10 microns and average widths of 100 microns are typical values for the aluminum substrates which were measured and are consistent with the requirement that the surface slopes be small. Examination of the surfaces under a microscope indicated that the facet surfaces were sharp edged. Thus, the surfaces were electropolished to remove 30 μ -inches from the facet edges as has been the procedure of other experimenters.

Preliminary measurements were made manually. The aspect angle of the target surface, the orientation of the K-rotator and the Brewster angle polarizer were reset by hand for each data point. The laser beam and optic axis of the detector set-up subtended equal angles with the target normal. Thus at 0° aspect angle, the laser beam and detector were set at $\theta_i = \theta_s$ and $\phi_s = 0$ (specular angle).

The advantage of such an experimental configuration, in addition to the simplification obtained in transforming from field angles to laboratory angles, is that the aspect angle setting is a direct measure of the facet slope (assuming that the facet model of scattering from rough surfaces is valid).

The first set of measurements, in which the depression angle was steep, $\xi = 7.6^\circ$, were in excellent agreement with the predictions of the facet model, as far as the location of the HH null. Theory predicts that the β_{HH} null is given by: (see equation [2] of reference 5)

$$\cos(\phi) = \frac{\sin^2(\theta)}{1 + \cos^2(\theta)} \quad (34)$$

when the incident and scattered polar angles have the same value. In terms of the laboratory coordinates, Setting $\eta = 2\xi + 90^\circ$ in equation (21), and expressing (21) in terms of the laboratory angles, given in Eqn. (20), (21), and (28), (34) can be written as:

$$\frac{\sin^2(\xi) - \cos^2(\xi) \sin^2(\Psi)}{1 - \cos^2(\xi) \cos^2(\Psi)} = \frac{1 - \cos^2(\xi) \cos^2(\psi)}{1 + \cos^2(\xi) \cos^2(\psi)} \quad (35)$$

For $\xi = 7.6^\circ$, the HH signal vanishes at $\psi = 7.5^\circ$ (Figure 6).

A systematic search was subsequently made for other HH nulls. Specifically, starting with $\xi = 10^\circ$, data were collected up to $\xi = 60^\circ$ in 10° increments. The position of the HH null as a function of aspect angle increases with increasing depression angle ξ . It ranges from $\psi = 9^\circ$ when $\xi = 10^\circ$ to $\psi = 43^\circ$ when $\xi = 60^\circ$ (Figures 6-19).

IV. Data and Results of Preliminary Measurements for Roughened Metallic Surfaces

The following data were collected using the experimental set up described in Figure 5. For each data set which follows, the depression angle was fixed and the aspect angle allowed to vary through a range of angles which included a predicted null position. The six data sets each represent a different, fixed value for the depression angle incremented by 10° from 10° to 60° . Data plots of the scattered cross section $\sigma_o(HH)$ and the ratios $\sigma_o(HH)/\sigma_o(HV)$ are given for each depression angle. In Figure 21, the data taken for a depression angle of 60° is plotted along with the model predictions for different facet slopes, S/T , where S is the average facet depth and T is the average facet spacing. To test theoretical prediction against experimental results, we compared $R_{\text{theoretical}} = \sigma_{HH}(\psi)/\sigma_{HH}(\psi_o)$ with $R_{\text{experimental}} = I_s(\psi)/I_s(\psi_o)$, where ψ_o is the smallest aspect angle for which data was recorded at a fixed depression angle and $I_s(\psi)$ is the scattered intensity. Figures 22-28 indicate the degree of fit between the modeled and measured values of $\sigma_o(HH)$.

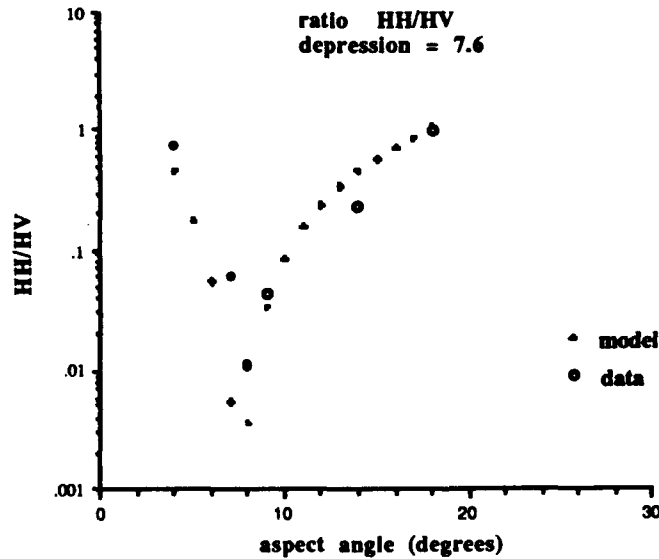


Figure 6. $\sigma_o(HH)/\sigma_o(HV)$ for a depression angle of 7.6°

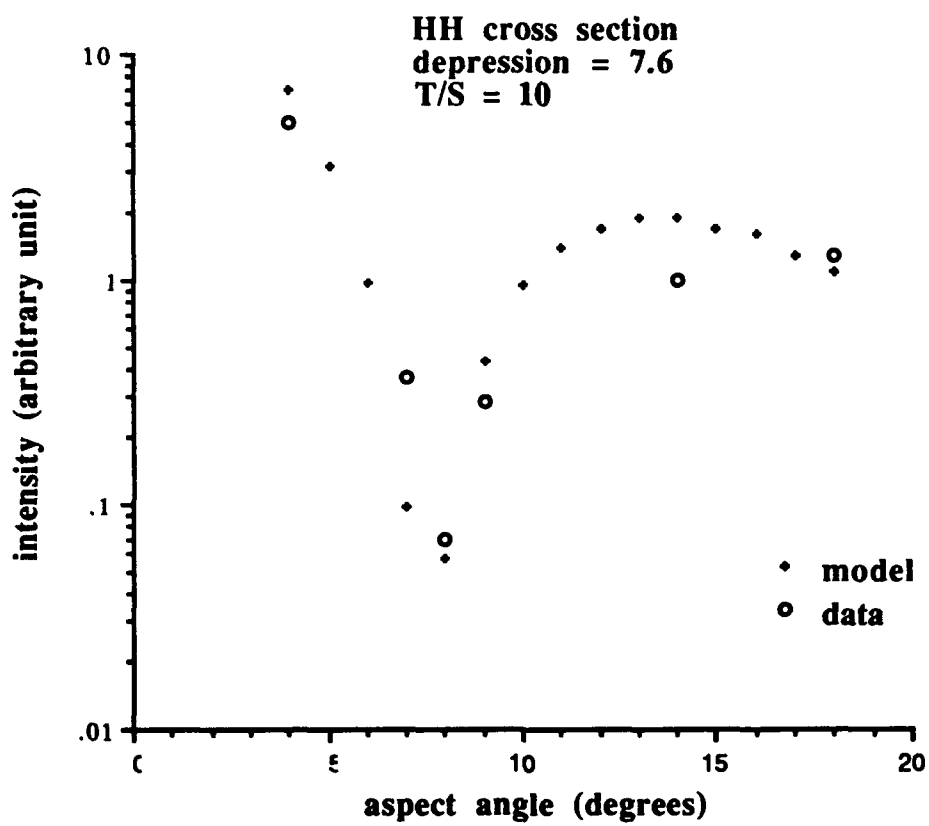


Figure 7. $\sigma_0(\text{HH})$ for a depression angle of 7.6°

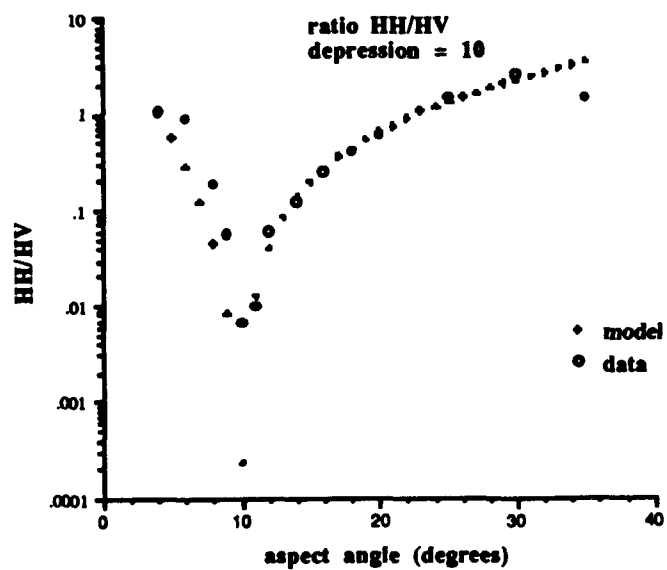


Figure 8. $\sigma_0(\text{HH})/\sigma_0(\text{HV})$ for a depression angle of 10°

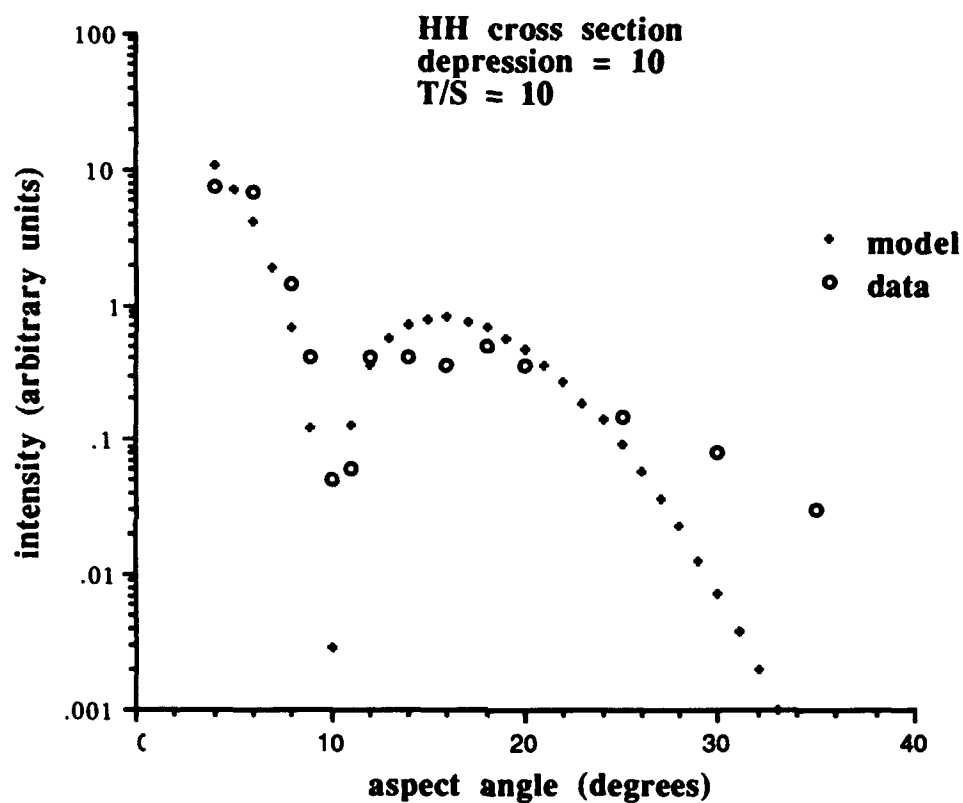


Figure 9. $\sigma_0(\text{HH})$ for a depression angle of 10°

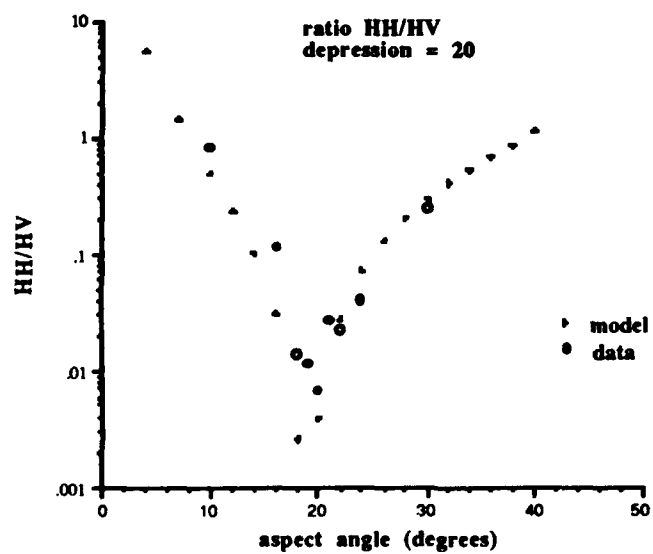


Figure 10. $\sigma_0(\text{HH})/\sigma_0(\text{HV})$ for a depression angle of 20°

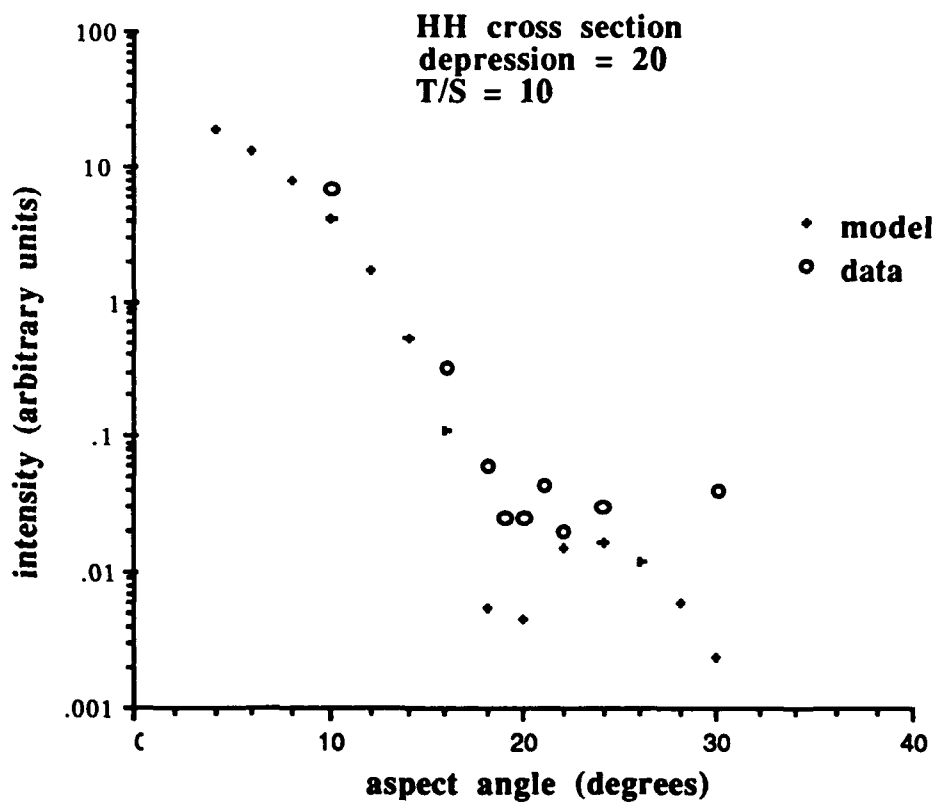


Figure 11. $\sigma_0(\text{HH})$ for a depression angle of 20°

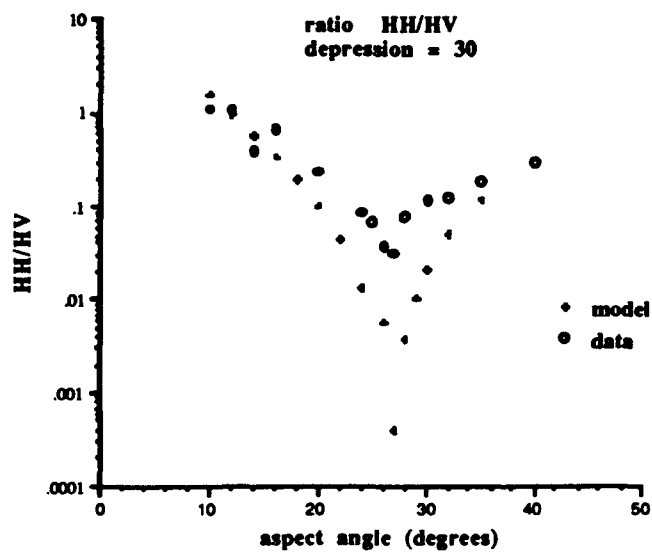


Figure 12. $\sigma_0(\text{HH})/\sigma_0(\text{HV})$ for a depression angle of 30°

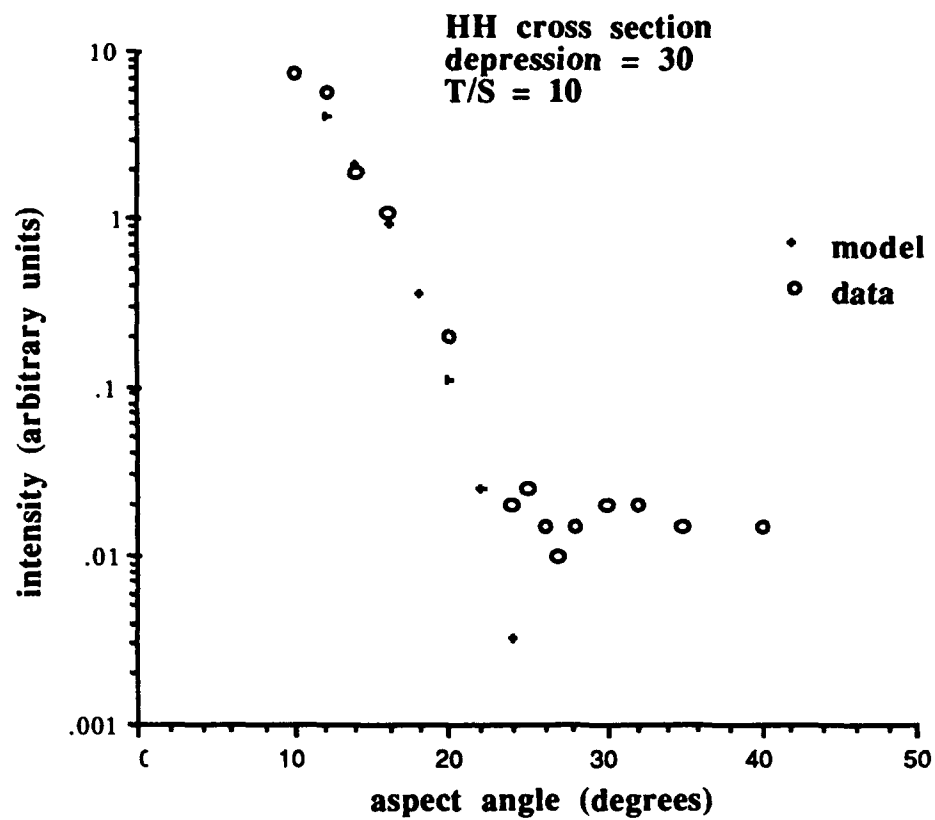


Figure 13. $\sigma_0(\text{HH})$ for a depression angle of 30°

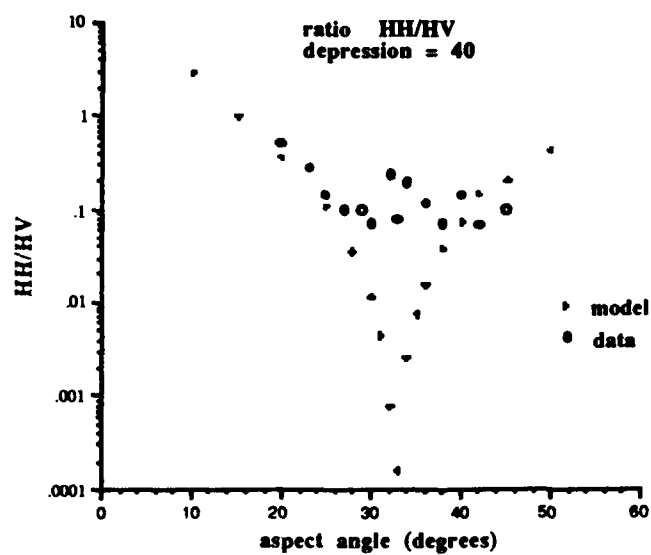


Figure 14. $\sigma_0(\text{HH})/\sigma_0(\text{HV})$ for a depression angle of 40°

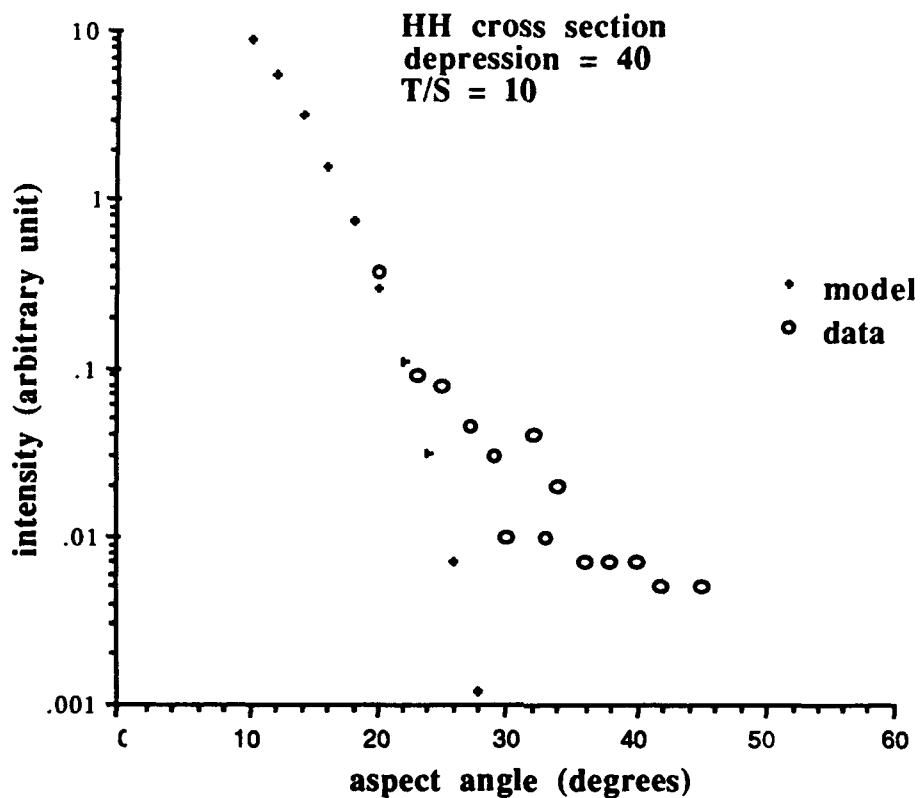


Figure 15. $\sigma_0(\text{HH})$ for a depression angle of 40°

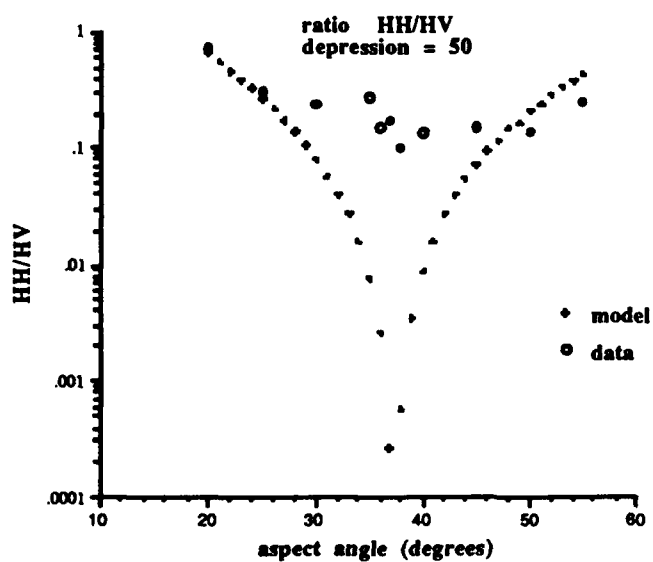


Figure 16. $\sigma_0(\text{HH})/\sigma_0(\text{HV})$ for a depression angle of 50°

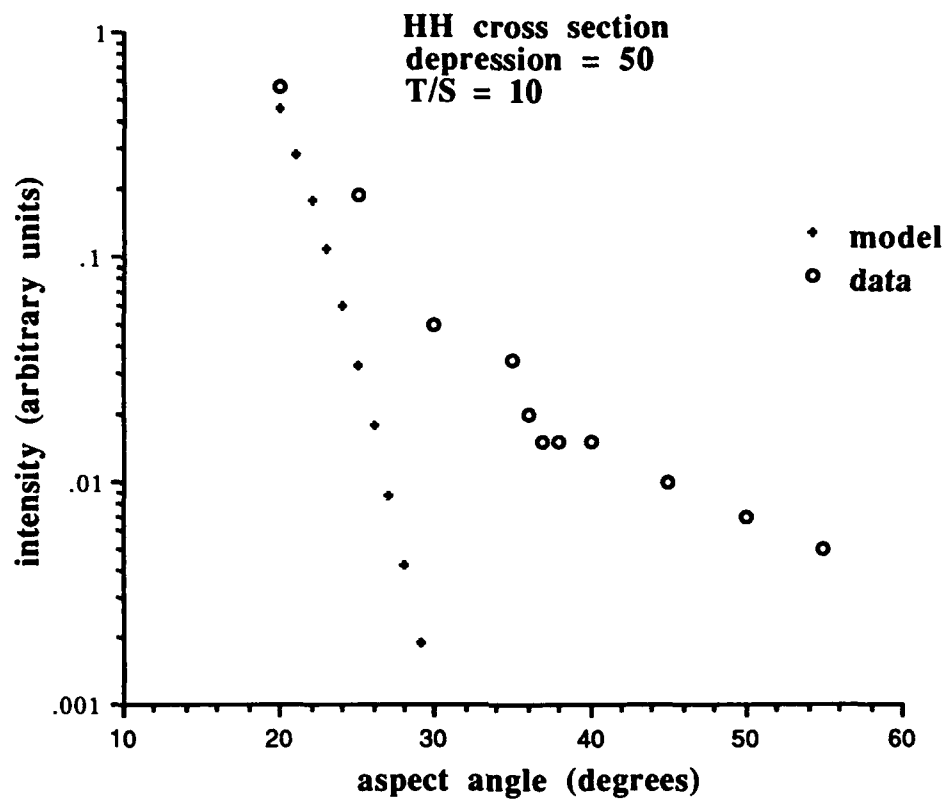


Figure 17. $\sigma_0(\text{HH})$ for a depression angle of 50°

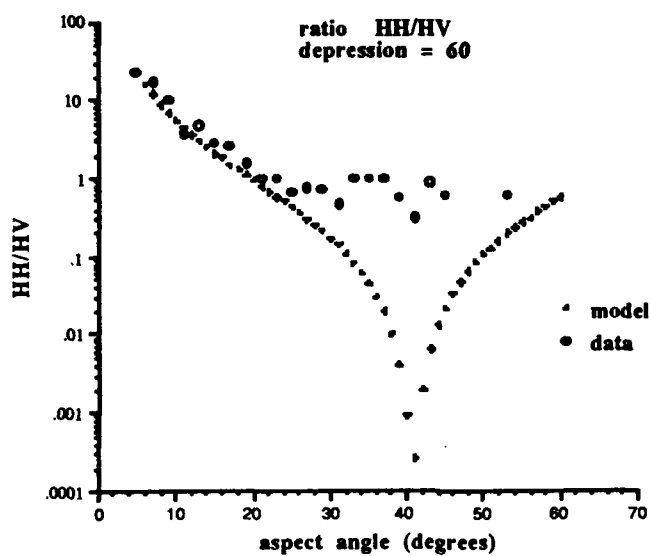


Figure 18. $\sigma_0(\text{HH})/\sigma_0(\text{HV})$ for a depression angle of 60°

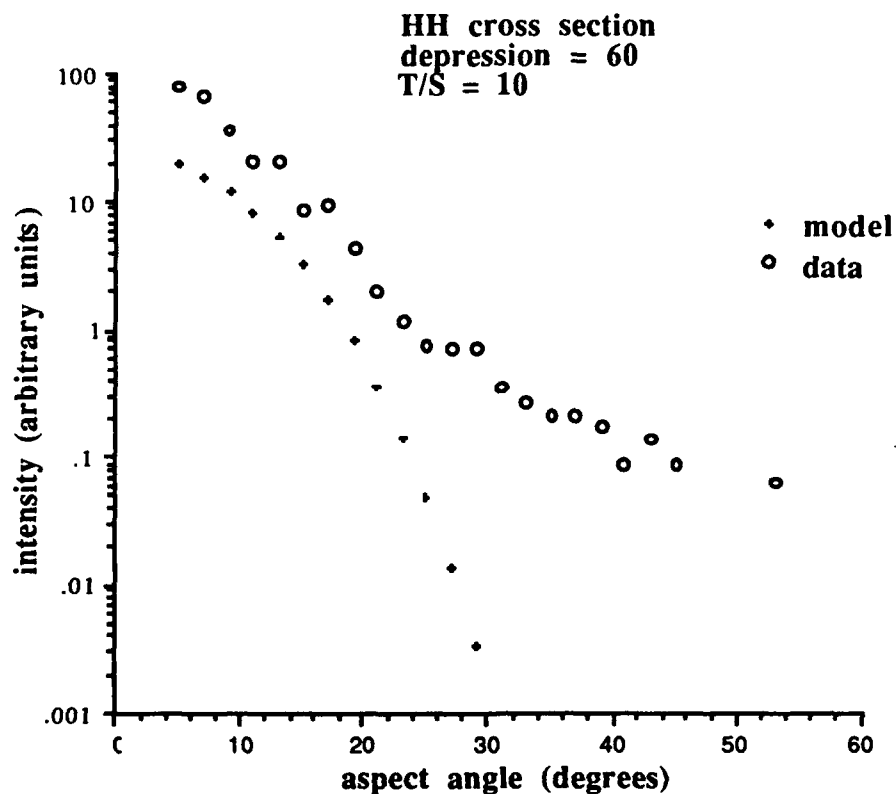


Figure 19. $\sigma_o(\text{HH})$ for a depression angle of 60°

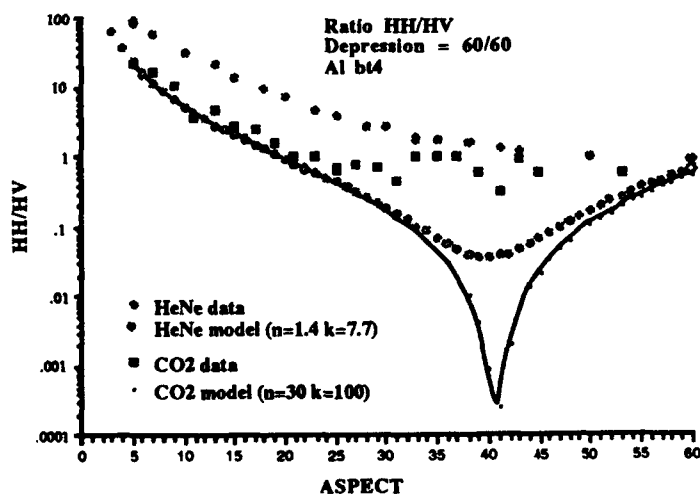


Figure 20. Ratio of HH/HV at 10.6 and 0.63 microns at a depression angle = 60°

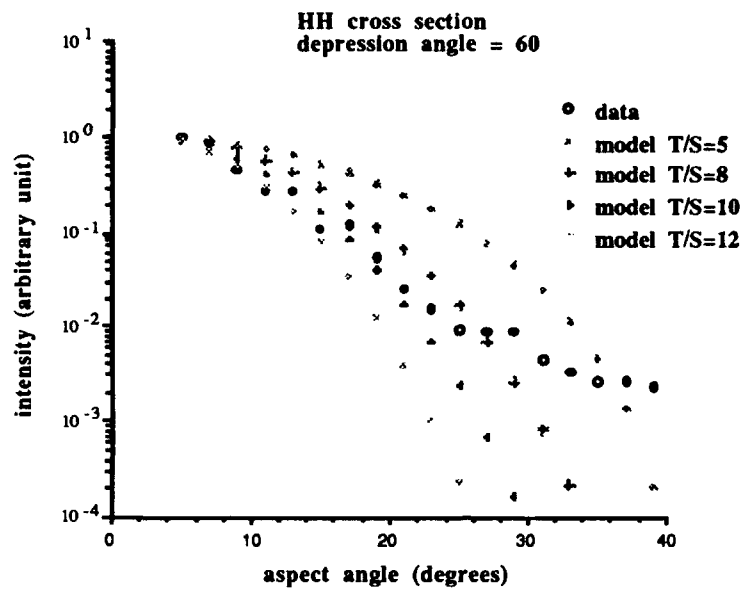


Figure 21. HH cross section at 60° depression for different facet slopes.

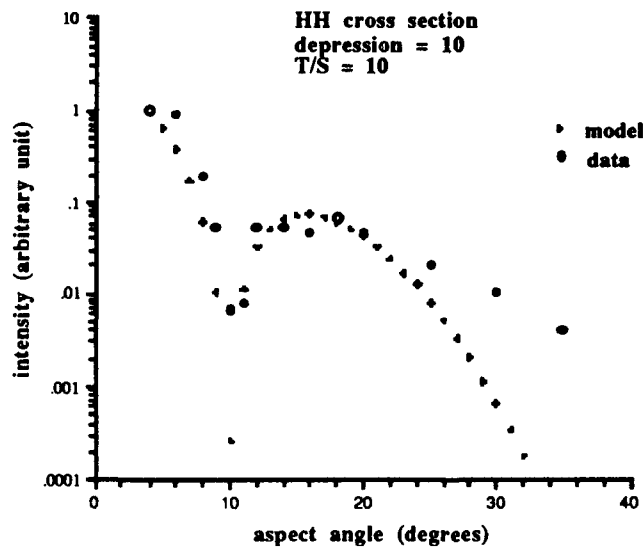


Figure 22. HH cross section and model normalized to unity.

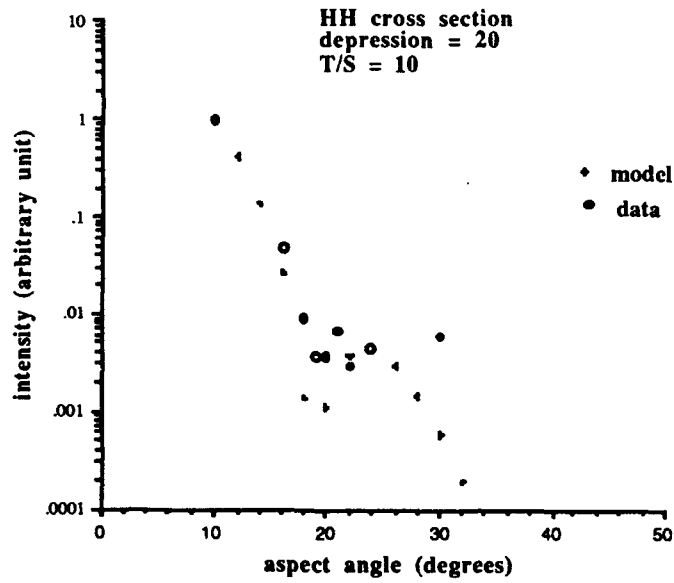


Figure 23. HH cross section and model normalized to unity.

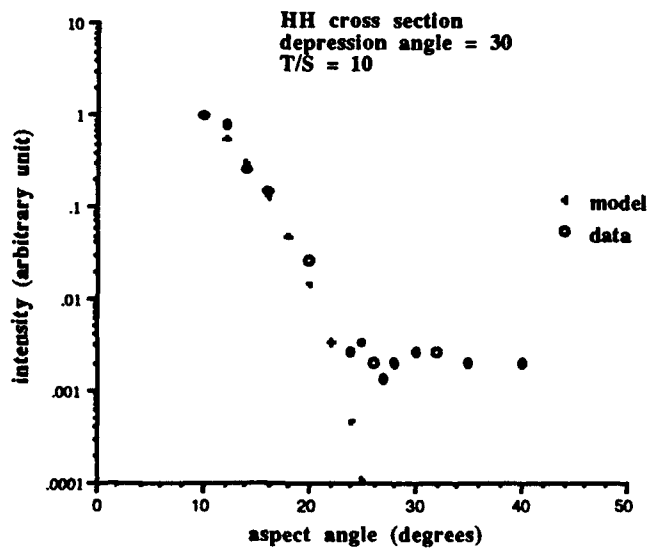


Figure 24. HH cross section and model normalized to unity.

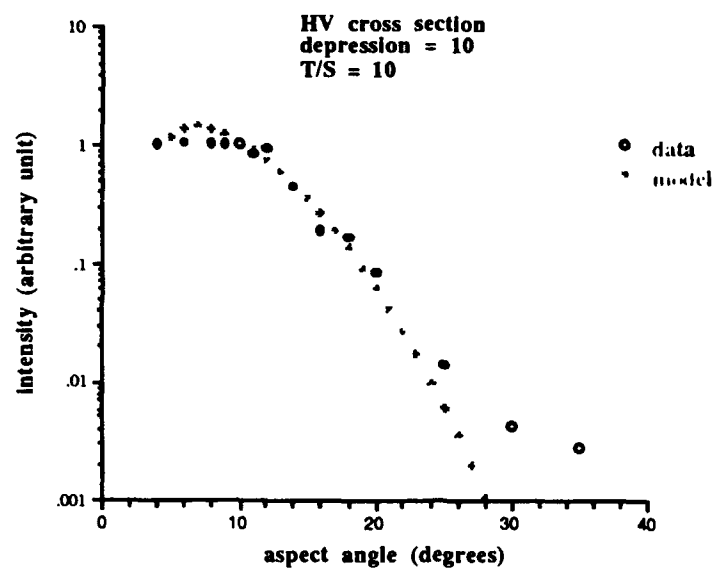


Figure 25. HH cross section and model normalized to unity.

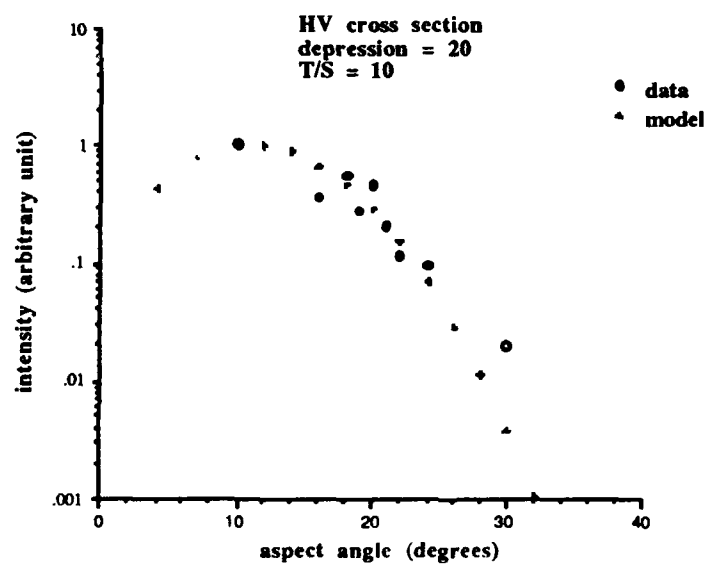


Figure 26. HV cross section and model normalized to unity.

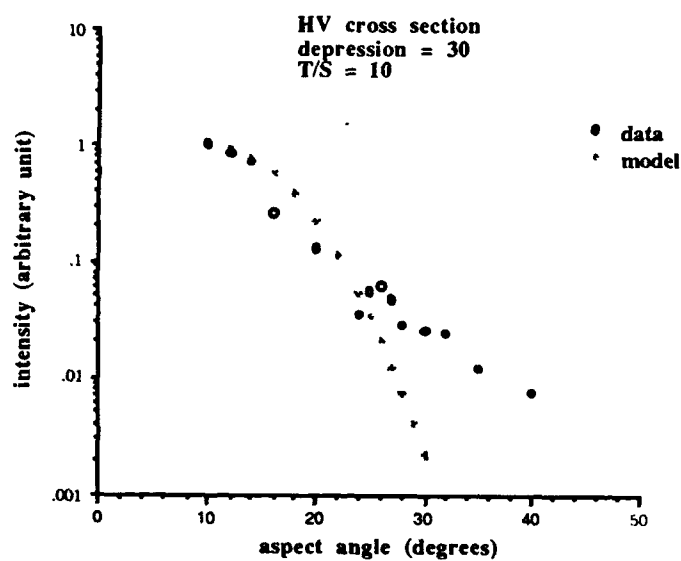


Figure 27. HV cross section and model normalized to unity.

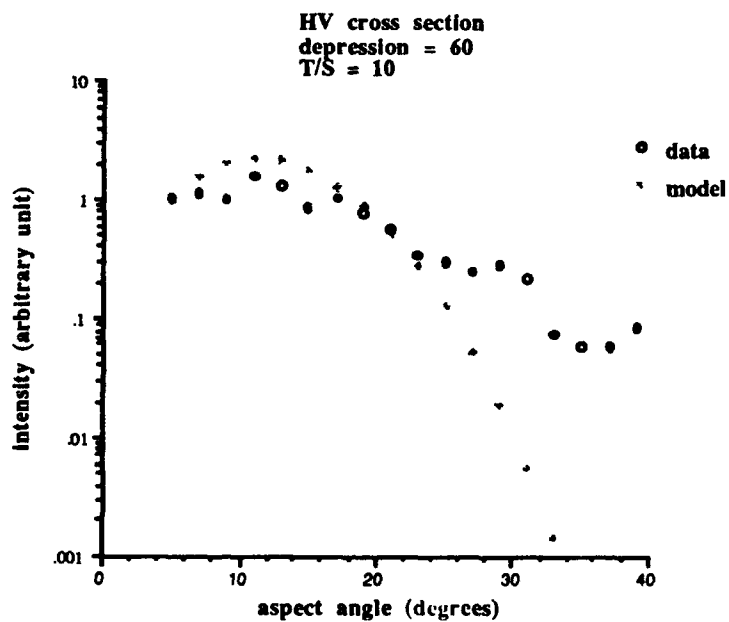


Figure 28. HV cross section and model normalized to unity.

V. Summary of Results

Surveying the data we conclude that excellent agreement is obtained between theory and experiment when ξ and ψ are small. For large ξ and ψ , theory and experimental values diverge.

Looking at the data in a systematic manner, it appears that the theoretical predictions, as applied to the roughened aluminum surfaces at a wavelength of 10.6 microns, break down at approximately $\psi = 25^\circ$, independent of depression angle ξ .

To avoid issues related to the degree of randomness of the surface, it is useful to plot the ratio of $(\sigma_o(HH)/\sigma_o(HV))$ and compare it to theory. According to the facet model, this ratio is independent of the distribution of facets. Thus⁵,

$$\frac{\sigma_o(HH)}{\sigma_o(HV)} = \frac{|\beta_{HH}|^2}{|\beta_{HV}|^2} \quad (36)$$

Whether the target surface has the correct number of facets with a given orientation is immaterial as far as this ratio is concerned. The important thing is that the surface has some facet with an orientation (ξ, ψ) . Thus, the existence of a scattering signal at a given aspect angle, attests to the existence of a corresponding facet.

Measurements were made for $\xi = 60^\circ$ and aspect angles ψ ranging from 5° to 50° . The ratio obtained from the data was compared to the theoretical prediction. Again theory and data agree for small aspect angles $\psi < 22^\circ$, and disagree for $\psi > 25^\circ$ (Figures 6-19).

There are several caveats in the derivation of the facet model, e.g., neglect of multiple scattering, wavelength independence of the result, in addition to the assumption of surface randomness.

To help delineate the significant complicating factors, it would be useful to measure the wavelength dependence (if any) of the data.

To this end, measurements of the ratio $\sigma_o(HH)/\sigma_o(HV)$ were remade using a HeNe laser source (633 nm). For this wavelength, theoretical and measured values disagree even at low values of ψ (Figure 20). The HeNe line has a wavelength of approximately 1/16 of the CO₂ line. The breakdown here may result partly from the increased probability of multiple scattering, since average groove depths are now approximately 10-15 λ , or as a result of a totally different roughness scale seen by shorter wavelength radiation. A more promising region for additional

study of these surfaces would be in the vicinity of 5 microns, i.e. at half the wavelength of the present measurements. The CO laser which operates at 5 microns is a potential radiation source.

Acknowledgment

We wish to thank Ms. M. Yoon for her invaluable assistance in data collection and analysis.

References

1. Petr Beckmann, Andre Spizzichino, "The Scattering of Electromagnetic Waves from Rough Surfaces", Pergamon, New York, 1963
2. ibid, pg. 178
3. Victor Twersky, "On Scattering and Reflection of Electromagnetic Waves by Rough Surfaces", IEEE Transactions on Antennas and Propagation, January, 1953
4. Donald E. Barrick, "Rough Surface Scattering Based on the Specular Point Theory", IEEE Transactions on Antennas and Propagation, Vol. AP-16, No.4, July, 1968
5. Robert J. Papa, John L. Lennon, Richard L. Taylor, "The Variation of Bistatic Rough Surface Scattering Cross Section for a Physical Optics Model", IEEE Transactions on Antennas and Propagation, Vol. AP-34, No.10 October, 1986
6. J. Renau, P. K. Cheo, and H. G. Cooper, "Depolarization of Linearly Polarized EM Waves Backscattered from Rough Metals and Inhomogeneous Dielectrics", Journal of the Optical Society of America, Vol. 57, No.4, April, 1967
7. Maurice I. Sancer, "Shadow Corrected Electromagnetic Scattering from Randomly Rough Surfaces", IEEE Transactions on Antennas and Propagation, Vol. AP-17, No.5, September, 1969



MISSION

of

Rome Air Development Center

RADC plans and executes research, development, test and selected acquisition programs in support of Command, Control, Communications and Intelligence (C³I) activities. Technical and engineering support within areas of competence is provided to ESD Program Offices (POs) and other ESD elements to perform effective acquisition of C³I systems. The areas of technical competence include communications, command and control, battle management information processing, surveillance sensors, intelligence data collection and handling, solid state sciences, electromagnetics, and propagation, and electronic reliability/maintainability and compatibility.